Published in final edited form as:
Inhal Toxicol. 2009 May ; 21(6): 512–518. doi:10.1080/08958370802598005.

Magnetic resonance imaging and computational fluid dynamics (CFD) simulations of rabbit nasal airflows for the development of hybrid CFD/PBPK models

R. A. Corley[1], **K. R. Minard**[1], **S. Kabilan**[1], **D. R. Einstein**[1], **A. P. Kuprat**[1], **J. R. Harkema**[2], **J. S. Kimbell**[3], **M. L. Gargas**[4], and **John H. Kinzell**[5]

[1] Battelle, Pacific Northwest Division, Richland, Washington

[2] Michigan State University, East Lansing, Michigan

[3] The Hamner Institutes for Health Sciences, Research Triangle Park, North Carolina

[4] The Sapphire Group, Inc., Beavercreek, Ohio

[5] Arysta Life Sciences, North America, San Francisco, California, USA

Abstract

The percentages of total airflows over the nasal respiratory and olfactory epithelium of female rabbits were calculated from computational fluid dynamics (CFD) simulations of steady-state inhalation. These airflow calculations, along with nasal airway geometry determinations, are critical parameters for hybrid CFD/physiologically based pharmacokinetic models that describe the nasal dosimetry of water-soluble or reactive gases and vapors in rabbits. CFD simulations were based upon three-dimensional computational meshes derived from magnetic resonance images of three adult female New Zealand White (NZW) rabbits. In the anterior portion of the nose, the maxillary turbinates of rabbits are considerably more complex than comparable regions in rats, mice, monkeys, or humans. This leads to a greater surface area to volume ratio in this region and thus the potential for increased extraction of water soluble or reactive gases and vapors in the anterior portion of the nose compared to many other species. Although there was considerable interanimal variability in the fine structures of the nasal turbinates and airflows in the anterior portions of the nose, there was remarkable consistency between rabbits in the percentage of total inspired airflows that reached the ethmoid turbinate region (~50%) that is presumably lined with olfactory epithelium. These latter results (airflows reaching the ethmoid turbinate region) were higher than previous published estimates for the male F344 rat (19%) and human (7%). These differences in regional airflows can have significant implications in interspecies extrapolations of nasal dosimetry.

Nasal tissues can be a target for a variety of volatile compounds following inhalation exposures. The potential for and regional distribution of nasal lesions generally reflect species differences in the distribution of specific epithelial cell types, metabolic capacity, nasal mucociliary apparatus, and intranasal airflow patterns (Harkema, 1990; Morgan & Monticello, 1990). Appropriately extrapolating the “dose” to target tissues observed in nasal airways of animals used in inhalation toxicity studies to humans must therefore factor these and potentially other differences in anatomy and physiology to improve human health risk assessments. As a result, three-dimensional computational fluid dynamic (CFD) models of the nasal airways of the male

Address for Correspondence: Richard A. Corley, PhD, Biological Monitoring & Modeling Group, Battelle, Pacific Northwest Division, 902 Battelle Blvd.. Mail Stop P7-59, Richland, WA 99352, USA. rick.corley@pnl.gov.

Declaration of interest: The authors report no conflicts of interest.

F344 rat, rhesus monkey, and human were developed to improve estimates of species-specific localized dosimetry in nasal tissues (Kimbell et al., 1993, 1997; Kepler et al., 1998; Subramaniam et al., 1998). These models have since been linked with physiologically based pharmacokinetic (PBPK) models to include systemic distribution of several volatile organic chemicals and their metabolites (Andersen et al., 1999, 2000; Bush et al., 1998; Frederick et al., 1998, 2002).

Since methyl iodide (MeI) has been proposed as a non-stratospheric ozone-depleting pre-plant soil fumigant, it has undergone extensive inhalation toxicity testing. In several of these studies, nasal irritation and thyroid effects have been observed in rats and late-term (gestation day [gd] 23–26) resorptions and thyroid effects have been observed in rabbits depending upon the exposure concentration, the duration and/or timing of exposure (Chamberlain et al., 1998; Kirkpatrick, 2002; Himmelstein et al., 2009; Nemec et al., 2009; Sloter et al., 2009). Extrapolations of the portal of entry (nose) and systemic dosimetry of MeI and its metabolite, iodide, can be accomplished using the anatomical and physiological framework from previous hybrid CFD/PBPK models developed for rats and humans. However, no such model currently exists for rabbits. Furthermore, advances in imaging, data analysis, and computational capabilities have led to significant improvements in the time required to develop computable three-dimensional (3D) meshes and the determination of localized airflow patters. As a result, it is now feasible to develop models from multiple animals to begin to understand the potential impact of variability in airway geometries. Therefore, the purpose of this study was to exploit these recent technologies to develop 3D nasal CFD models for three female New Zealand White (NZW) rabbits. The resulting models will be used to determine airflow splits to different regions of the nasal airways along with corresponding regional surface areas and volumes necessary to construct a hybrid CFD/PBPK model in this species.

Materials and methods

Chemicals

The magnetic resonance contrast agent Magnevist (lot 644982T) was obtained from Berlex Laboratories (Wayne, NJ). Each milliliter of Magnevist contained 469.01 mg gadopentetate dimeglumine, 0.99 mg meglumine, and 0.40 mg diethylenetriamine pentaacetic acid and was utilized undiluted. Ketamine (Keta-Thesia) was obtained from Phoenix Scientific (St. Joseph, MO); xylazine (Cervizine) was obtained from Wildlife Pharmaceuticals (Fort Collins, CO); acepromazine maleate was obtained from Boerhinger Ingelheim (St. Joseph, MO); and Euthanasol (390 mg pentobarbital sodium + 50 mg phenytoin sulfate/ml) was obtained from Virbac Animal Health, Inc. (Fort Worth, TX).

Preparation of animals

Naive female New Zealand White rabbits, approximately 4–5 kg body weight (5–6 mo of age), were obtained from Western Oregon Rabbit Company (Philomath, OR). Upon arrival at the laboratory, the animals were individually housed in wire-bottomed cages with polycarbonate resting boards and were acclimated in a humidity- and temperature-controlled room with a 12-h light/dark cycle for at least 1 wk prior to use. Each rabbit was provided certified high-fiber rabbit feed (PMI Nutrition, Richmond, IN) and water *ad libitum*. Diets were supplemented with Timothy hay cubes (Oxbow Hay Co., Murdock, NE).

In preparation for magnetic resonance (MR) imaging, each rabbit was weighed and anesthetized using a subcutaneous injection of ketamine (35 mg/kg), xylazine (5 mg/kg), and acepromazine (0.75 mg/kg) mixture. Once anesthetized, a butterfly needle (23 gauge) was inserted into an ear vein for injection of Magnevist (0.3 ml/kg corresponding to 140 mg/kg) and, after ~10 min, the animal was euthanized with an overdose of Euthanasol (100 mg/kg).

The head was removed, placed in the imaging probe, and maintained at ~4°C until the imaging was completed.

This study was performed according to the "Guide for the Care and Use of Laboratory Animals" (National Research Council, Washington DC, 1996). The protocol for administration of anesthesia, the magnetic resonance contrast agent, and euthanasia was approved by the Institutional Animal Care and Use Committee at Pacific Northwest National laboratory.

Magnetic resonance (MR) imaging

Rabbits were imaged using an adaptation of methods previously developed in this laboratory for rats (Timchalk et al., 2001; Minard et al., 2006). In this study, magnetic resonance (MR) imaging was performed using a 2.0-tesla horizontal-bore magnet, a Varian Unity Plus console (Varian, Inc., Palo Alto, CA), and a custom, in-house fabricated linearly polarized birdcage coil with an 8-cm inner diameter. During imaging, the sample temperature was maintained at ~4°C. After each sample was positioned in the magnet bore, two-dimensional (2D) MR imaging was performed to define a 3D reference frame aligned with the major symmetry axis of nasal airway tissues. High-resolution MR images were then collected using a 3D spin echo characterized by an echo time of 15 ms, 2 averages, and a repetition time of 0.15 s. Raw 3D MR data were collected on a 256 × 256 × 256 matrix in 5.5 h. After data collection, the image data was reconstructed using an unweighted Fourier transform on a 512 × 512 × 256 matrix covering an 8 × 8 × 16 cm field of view (FOV). Afterward, image data were stored as 256 2D slices that each showed a different 8 × 8 cm FOV. Each 625-μm-thick slice was stored as an 8-bit tiff file that contained 512 × 512 points.

Nasal airway segmentation

Each set of 256 tiff files was extracted by Digital Data Viewer (DDV; CGC Consulting, Placitas, NM; http://www.cgc-code.org) using *x*- and *y*-intervals of 1 and a *z*-interval of 4 to render the data in the proper aspect ratio and saved as a compiled DDV file. Airways were identified and segmented from each set of MR images after correction of poorly resolved data using the pixel editing tool available in DDV and subsequent flooding of regions of interest using a connected threshold algorithm (Yoo, 2004). The isosurface of each airway was then extracted from the segmented image data. To extract the isosurface, the regions "inside" and "outside" of nasal airways were associated with distinct real number values and a variant of the marching cubes algorithm (Sethian, 1996) was applied. For those airways that were convoluted and in places under-resolved, the generated surface was systematically checked for topological correctness and rectified, where necessary using the pixel-editing tool of DDV. After this process was repeated for the entire data set, an isosurface for the entire volume was generated and saved in the AVS UCD format (http://www.avs.com). This surface was then smoothed using volume-conserving smoothing (Kuprat et al., 2001) to enhance the features of the geometry to be meshed.

Computational mesh generation

The Los Alamos Grid Toolbox (LaGriT; http://lagrit.lanl.gov/) was used to generate finite-volume computational meshes of each rabbit nasal airway by an advancing front algorithm and Delaunay tetrahedralization. To ensure that even the smallest airway (only one voxel wide) had at least six nodes across the mesh to accurately capture the characteristics of fluid flow, the final smoothed isosurface generated from DDV was repeatedly offset (up to three times) normal to the boundary based upon the voxel dimensions. The points generated by repeated offsetting were placed inside and tested against the original isosurface from DDV. Any node lying outside of the isosurface was deleted. Thereafter, the complete nodal distribution was connected using a Delaunay algorithm. Another inside–outside test was performed and all the elements lying outside the isosurface were deleted. The resulting volume mesh was smoothed

two times using the minimum error gradient adaptation technique (MEGA) (Kuprat, 1995), which prevents mesh folding and self-intersection, and produces nearly isotropic elements when not used to adapt to a specific field variable. From this computational mesh, geometric information such as the length, volume, and surface areas were calculated for each rabbit nasal airway.

Computational fluid dynamics (CFD) simulations of airflows

Steady-state inhalation conditions were simulated with the Navier–Stokes equations using a commercial finite-volume solver Star-CD (http://www.cd-adapco.com). The inlet boundary condition was a prescribed volumetric flow rate of 680 ml/min, an average resting ventilation rate determined by whole-body plethysmography in a companion study (Thrall et al., 2009), while the outlets were prescribed a pressure boundary condition with a static pressure of zero. The nasal airway walls were assumed to be rigid and hairless with no-slip boundary conditions, and occlusive effects of potential nasal cycling were ignored. The steady, incompressible continuity, and momentum equations were solved with a second-order monotone advection and reconstruction scheme (MARS), using an algebraic multigrid (AMG) approach. The pressure–velocity coupling was accomplished using the SIMPLE method. The simulation was run on an SGI Altix 3000 server consisting of 128 Intel Itanium Family Processors running the Linux operating system in a single global shared memory architecture. Graphical displays of the resulting computational meshes and CFD simulations were generated using Tecplot (http://www.tecplot.com).

Calculation of flow splits for the hybrid CFD/PBPK model

To determine the flow splits of airflows targeting the major regions of nasal airways lined with respiratory versus olfactory epithelium, the nasal passages of each rabbit were partitioned into five regions using Tecplot based upon anatomical location and the type of epithelium (Negus, 1958) (Figure 1). The partitions identified in Tecplot were then exported to LaGriT to calculate the surface areas and volumes of each region and mass fluxes of airflows moving across each plane shown in Figure 1.

Results

Each female rabbit was successfully imaged using the Magnevist contrast agent and their nasal airways were segmented for the development of computational meshes. The nasal airway geometries (total volume, length and surface areas) were calculated from each computational mesh (Table 1). While the overall geometric characteristics were reasonably consistent across the three rabbits, there were a number of individual differences and asymmetries in the fine architecture of the nose. For example, rabbit 1 had a mass in the left maxilloturbinate that disrupted the turbinates, while rabbit 3 had a deviated septum in the posterior region of the nasal airways (Figure 2).

The volume meshes produced for each rabbit nasal airway consisted of ~5.2 million tetrahedral elements with over 95% of the tetrahedra having aspect ratios <10.0, with aspect ratio being defined as the ratio of the longest edge to the shortest edge in any given face of a tetrahedral. The quality of the meshes was largely due to the application of the MEGA smoothing algorithm that prevents mesh folding and self-intersection, and produces nearly isotropic elements (Kuprat, 1995). In addition, the initial placement of offset surface nodes (described in the Methods section) assured a minimum of six nodes across the smallest airways.

CFD simulations of steady-state inhalation utilized a global convergence tolerance of 1.0×10^{-4} for the momentum and mass residuals. Convergence was obtained after an average of 227 iterations on eight processors, taking a total wall-clock time of 2 h and 40 min (56000 sec CPU

time). Rapid convergence suggests that our adoption of the MARS algorithm was successful. The MARS differencing scheme is a two-step scheme with second-order accuracy and is relatively insensitive to errors resulting from mesh structure and skewness. It is thus suited to the hybrid unstructured meshes that our meshing approach produces.

As shown in projected contour maps of the cross-sectional absolute velocity of airflows (Figure 3), the majority of the inhaled air enters the nostril dorsally, where it distributes relatively evenly through the maxilloturbinates in the anterior portion of the nose. Once the airflows reach the end of the maxilloturbinates, the major flows are either directed ventrally toward the nasopharynx or pass through the forward dorsal projections of the ethmoid turbinates (Figure 4) before also veering ventrally to enter the nasopharynx prior to reaching the posterior ethmoid turbinate region.

The resulting calculations of airflows entering each region of the nose were reasonably consistent across the three rabbits, with the biggest difference being the mass flux entering the anterior maxilloturbinate region of rabbit 1 (Table 2). However, even with the higher calculated airflows entering the anterior ventral respiratory compartment (VR1) in rabbit 1 (17.6%) versus the other two rabbits (3.5–4.1%), the calculated airflows exiting the anterior dorsal respiratory (DR1) and ventral respiratory (VR1) compartments were remarkably similar across all three rabbits.

It is important to note that the airflow splits summarized in Table 2 were calculated as the percent of the total mass flux (kg/min) entering each compartment across each vertical cross-sectional or *z*-slice only and do not include crossovers between dorsal and ventral regions. The total airflows through each region are readily determined from these values by mass balance of airflows entering and leaving each region across each horizontal or vertical plane shown in Figure 1 such that the total flow is maintained at the steady-state input rate of 680 ml/min. For example, the total airflows exiting the ventral respiratory region (VR1) at *z*-slice b in Figure 1 (e.g., 0.526 × 680 ml/min = 357.7 ml/min) includes the air entering the ventral region of the cross-section z-slice a (e.g., 0.084 × 680 ml/min = 57.1 ml/min) plus part of the airflows from the dorsal respiratory region (DR) that does not continue dorsally into the posterior dorsal olfactory region (DO1) [(0.916–0.474) × 680 ml/min = 300.6 ml/min]. Similarly, the total airflow entering and leaving the posterior ventral respiratory region (VR2) into the nasopharynx includes airflows from the anterior ventral respiratory region (VR1; 357.7 ml/min, calculated above) plus flows from the anterior and posterior dorsal olfactory regions (DO1 and DO2) that add up to the total flow rate to maintain the mass balance of 680 ml/min.

Interestingly, the posterior dorsal olfactory compartment (DO2), which encompasses nearly 24% of the total surface area of the nose, received less than 2% of the total airflow entering the nose with the major source coming from the nasoturbinate, which transcends the dorsal most portion of the nose. The airflows that enter this region near the dorsal roof of this compartment are typically at very low velocities that initially continue toward the rear of the ethmoid turbinates before sweeping forward to exit near the entrance to the nasopharynx (Figures 3 and 4).

Discussion

In the anterior portion of the nose, the maxillary turbinates of rabbits are considerably more complex than comparable regions in rats, mice, monkeys, or humans. This leads to a greater surface area to volume ratio in this region and thus the potential for increased extraction of water soluble or reactive gases and vapors from airways in the anterior portion of the nose compared to other species. While the regional distribution of MeI uptake in the nasal airways of rabbits has not been determined, we have shown in a companion study (Thrall et al., 2009)

that slightly more MeI is taken up by nasal tissues in rabbits (72 ± 11%) than in rats (63 ± 8%), which likely reflects these anatomical differences.

Prior to this study, hybrid CFD-PBPK models have been developed using a single rat, monkey and human 3D/CFD model as the basis for nasal airflow simulations and regional airway extractions (Kimbell et al., 1997; Andersen et al., 1999; Frederick et al., 1998). With the application of new imaging and data segmentation methods such as those described herein, the opportunity to develop models based upon multiple animals is now feasible. Since the variability in nasal airway geometry has not been adequately characterized in rabbits (or any other species), three animals were arbitrarily selected as the initial basis for imaging and CFD model development. As shown in Table 2, there was a high degree of variability in airflow splits only in the most anterior portion of the nose of the three rabbits. Once the air was mixed in the maxilloturbinates, the airflows through each region of the nose were remarkably consistent across the three rabbits even though there were some marked structural differences identified (Figure 2). Regardless, these data point out the need for further characterization of animal and human variability, especially at various life stages, or disease states as technological advances have made this more feasible.

With regard to comparisons between rabbits and previously determined rat and human nasal compartmental airflow splits (Andersen et al., 1999, 2000; Bush et al., 1998; Frederick et al., 1998, 2002), the largest differences between species was observed in the anterior portion of the nose, which in rabbits, is dominated by highly intricate maxillary turbinates that significantly affects the airflows in this region. As summarized in Table 2, the highest airflow entering the anterior dorsal respiratory epithelium compartment (DR) was observed in rabbits (91.6 ± 8.0%), followed by the rat (15%) and human (8%). The opposite rank order was, by mass balance, observed in the ventral major airflow stream with the human at 92%, rat at 85%, and rabbit at 8.4 ± 8.0%. In the posterior nasal airways, the portion of the total airflows that targeted the anterior olfactory epithelium compartment (DO1) of the rabbits (47.4 ± 4%) was considerably greater than previous determinations for the rat (19%), both of which are considerably higher than the human (7%). However, the airflows reaching the posterior ethmoid turbinates were considerably lower in the rabbits (1.1 ± 0.8% vs. 17–21% for the rat). These differences in the posterior ethmoid turbinate flow rates are associated with the geometry, size, and positioning of the rabbit ethmoid turbinates relative to comparable regions in the rat. These anatomical differences impacted CFD simulations of localized flow stream patterns (see Figures 3 and 4) in the rabbit ethmoid region, which warranted a subdivision (slice c in Figure 1) of the olfactory regions into an anterior region that is in close proximity to the maxillary turbinates and the region posterior to the junction with the nasopharynx. Such species differences in anatomy and regional airflows ventilating different nasal epithelial cell types can have significant implications for extrapolating human inhalation risks from animal studies, as has been shown for a variety of water-soluble, highly metabolized, or reactive gases and vapors (Andersen et al., 1999, 2000, 2002; Bogdanffy et al., 1999; Frederick et al., 1998, 2002; Kimbell et al., 2001a, 2001b; Kimbell & Subramanian, 2001; Sweeney et al., 2008).

Future studies on CFD modeling of the rabbit nasal airflows should consider more realistic breathing patterns to more thoroughly characterize the regional airflows and gas exchange during inhalation and exhalation in rabbits as well as in rats, monkeys and humans. Furthermore, airway geometry atlases and associated statistics, similar to those being developed for the human (Li et al., 2003), could be developed for the rabbit to address questions of variability in airway geometry and its potential impact on regional airflows if there are sufficient issues associated with intra- versus interspecies extrapolations. Likewise, the current compartmental boundaries used in this study to estimate airflow splits in the rabbit nasal passages were based primarily on gross morphological landmarks. These boundaries and associated airflow splits can be improved when detailed histological data become available to

more precisely map the distribution of specific airway epithelium cell types. Databases to construct such airway geometry atlases and airway epithelium maps are currently being developed for rats, mice, and monkeys in our respective laboratories, but, to our knowledge, no such maps are being developed for the rabbit.

The results from this initial development of 3D/CFD models for the rabbit provide a solid foundation for the development of a hybrid CFD/PBPK model for rabbits as described in the companion paper of Sweeney et al. (2009). This interface between the rabbit nasal and PBPK model can be considered generic and utilized for any chemical where nasal dosimetry in rabbits is an important consideration. Additional physiological and biochemical constants specific to the development of a PBPK model for MeI in rabbits are presented in Sweeney et al. (2009).

Acknowledgments

Research was performed in the Environmental Molecular Science Laboratory (a national scientific user facility sponsored by the US Department of Energy (DOE) Office of Biological and Environmental Research) located at Pacific Northwest National Laboratory (PNNL), and operated for DOE by Battelle. This work was funded by the Arvesta Corporation, San Francisco, CA, under BNW Project 47542. The MR imaging, airway segmentation, and computational methods were made possible by grants from the U.S. Department of Energy (Project 40403) and National Institutes of Health (NHLBI HL073598-01A1 and NIEHS ES011617).

References

Andersen ME, Green T, Frederick CB, Bogdanffy MS. Physiologically based pharmacokinetic (PBPK) models for nasal tissue dosimetry of organic esters: Assessing the state-of-knowledge and risk assessment applications with methyl methacrylate and vinyl acetate. Regul Toxicol Pharmacol 2002;36:1–12. [PubMed: 12383713]

Andersen ME, Sarangapani R, Frederick CB, Kimbell JS. Dosimetric adjustment factors for methyl methacrylate derived from a steady-state analysis of a physiologically based clearance-extraction model. Inhal Toxicol 1999;11:899–926. [PubMed: 10509026]

Andersen ME, Sarangapani R, Gentry R, Clewell H, Covington T, Frederick CB. Application of a hybrid CFD-PBPK nasal dosimetry model in inhalation risk assessment: An example with acrylic acid. Toxicol Sci 2000;57:312–325. [PubMed: 11006361]

Bogdanffy MS, Sarangapani R, Plowchalk DR, Jarabek A, Andersen ME. A biologically based risk assessment for vinyl acetate-induced cancer and noncancer inhalation toxicity. Toxicol Sci 1999;51:19–35. [PubMed: 10496674]

Bush ML, Frederick CB, Kimbell JS, Ultman JS. A CFD-PBPK hybrid model for simulating gas and vapor uptake in the rat nose. Toxicol Appl Pharmacol 1998;150:133–145. [PubMed: 9630462]

Chamberlain MP, Lock EA, Reed CJ. Investigations of the pathways of toxicity of methyl iodide in the rat nasal cavity. Toxicology 1998;129:169–181. [PubMed: 9772095]

Frederick C, Bush ML, Lomax LG, Black KA, Finch L, Kimbell JS, Morgan KT, Subramaniam RP, Morris JB, Ultman JS. Application of a hybrid computational fluid dynamics and physiologically based inhalation model for interspecies dosimetry extrapolation of acidic vapors in the upper airways. Toxicol Appl Pharmacol 1998;152:211–231. [PubMed: 9772217]

Frederick C, Lomax LG, Black KA, Finch L, Scribner HE, Kimbell JS, Morgan KT, Subramaniam RP, Morris JB. Use of a hybrid computational fluid dynamics and physiologically based inhalation model for interspecies dosimetry comparisons of ester vapors. Toxicol Appl Pharmacol 2002;183:23–40. [PubMed: 12217639]

Harkema JR. Comparative pathology of the nasal mucosa in laboratory animals exposed to inhaled irritants. Env Health Perspect 1990;85:231–238. [PubMed: 2116960]

Himmelstein MW, Kegelman TA, DeLorme MP, Everds NE, O'Connor JC, Kemper RA, Nabb DL, Mileson BE, Bevan C. Two-day inhalation toxicity study of methyl iodide in the rat. Inhal Toxicol 2009;21:480–487. [PubMed: 19519148]

Kimbell JS, Subramanian RP. Use of computational fluid dynamics models for dosimetry of inhaled gases in the nasal passages. Inhal Toxicol 2001;13:325–334. [PubMed: 11295865]

Kimbell JS, Godo MN, Gross EA, Joyner DR, Richardson RB, Morgan KT. Computer simulation of inspiratory airflow in all regions of the F344 rat nasal passages. Toxicol Appl Pharmacol 1997;145:388–398. [PubMed: 9266813]

Kimbell JS, Overton JH, Subramanian RP, Schlosser PM, Morgan KT, Conolly RB, Miller FJ. Dosimetry modeling of inhaled formaldehyde: Binning nasal flux predictions for quantitative risk assessment. Toxicol Sci 2001;64:111–121. [PubMed: 11606807]

Kimbell JS, Subramanian RP, Gross EA, Schlosser PM, Morgan KT. Dosimetry modeling of inhaled formaldehyde: Comparisons of local flux predictions in the rat, monkey, and human nasal passages. Toxicol Sci 2001;64:100–110. [PubMed: 11606806]

Kirkpatrick, DT. R&D Report WIL-418015. Ashland, OH: WIL Research Laboratories; 2002. A 13-week inhalation toxicity study (with a 4-week interim necropsy) of iodomethane in albino rats.

Kuprat, A. Los Alamos National Lab Report LAUR-95-1116. 1995. Adaptive smoothing techniques for 3-D unstructured meshes.

Kuprat A, Khamayseh A, et al. Volume conserving smoothing for piecewise linear curves, surfaces, and triple lines. J Comp Phys 2001;172:99–118.

Li B, Christensen GE, Hoffman EA, McLennan G, Reinhardt JM. Establishing a normative atlas of the human lung: Intersubject warping and registration of the volumetric CT images. Acad Radiol 2003;10:255–265. [PubMed: 12643552]

Minard KR, Einstein DR, Jacob RE, Kabilan S, Kuprat A, Timchalk C, Trease L, Corley RA. Application of magnetic resonance (MR) imaging for the development and validation of computational fluid dynamics (CFD) models of the rat respiratory system. Inhal Toxicol 2006;18:787–794. [PubMed: 16774868]

Morgan KT, Monticello TM. Airflow, gas deposition, and lesion distribution in the nasal passages. Environ Health Perspect 1990;85:209–218. [PubMed: 2200663]

Negus, V. The comparative anatomy and physiology of the nose and paranasal sinuses. London: Livingstone; 1958.

Nemec M, Sloter E, Stump D, Holson J, Kirkpatrick D, Kinzell J. Prenatal developmental toxicity studies of inhaled methyl iodide vapor in rabbits reveal a susceptible window of exposure inducing late gestational fetotoxicity. Inhal Toxicol 2009;21:449–461. [PubMed: 19519146]

Sethian, JA. Level set methods and fast marching methods. Cambridge: Cambridge University Press; 1996.

Sloter E, Nemec M, Stump D, Holson J, Kirkpatrick D, Gargas M, Kinzell J. Methyl iodide-induced fetal hypothyroidism implicated in late-stage fetal death in rabbits. Inhal Toxicol 2009;21:462–479. [PubMed: 19519147]

Subramaniam RP, Richardson RB, Morgan KT, Kimbell JS. Computational fluid dynamics simulations of inspiratory airflow in the human nose and nasopharynx. Inhal Toxicol 1998;10:91–120.

Sweeney LM, Andersen ME, Gargas ML. Ethyl acrylate risk assessment with a hybrid computational fluid dynamics and physiologically based nasal dosimetry model. Toxicol Sci 2004;79:394–403. [PubMed: 15056811]

Sweeney LM, Kirman CR, Gannon SA, Thrall KD, Gargas ML, Kinzell JH. Development of a physiologically based pharmacokinetic (PBPK) model for methyl iodide in rats, rabbits and humans. Inhal Toxicol 2009;21:552–582. [PubMed: 19519155]

Thrall KD, Woodstock AD, Soelberg JJ, Gargas ML, Kinzell JH, Corley RA. A real-time methodology to evaluate the nasal absorption of volatile compounds in anesthetized animals. Inhal Toxicol 2009;21:531–536. [PubMed: 19519153]

Timchalk C, Trease HE, Trease LL, Minard KR, Corley RA. Potential technology for studying dosimetry and response to airborne chemical and biological pollutants. J Toxicol Ind Health 2001;17:270–276.

Yoo, TS. Segmentation basics. In: Yoo, TS., editor. Insight into images: Principles and practices for segmentation, registration, and image analysis. AK. Peters, Ltd; 2004.

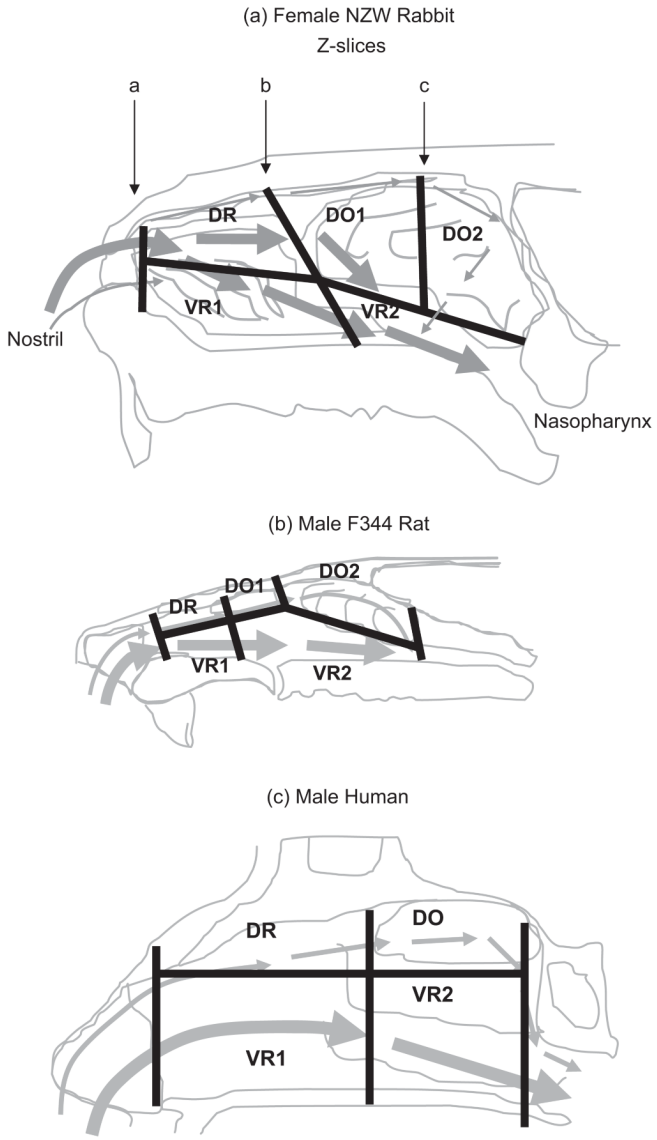

Figure 1.

(a) Division of rabbit nasal airways into five discrete regions based upon types of epithelium and main airflows. Slices along the *z* axis of the CFD model corresponded to the approximate borders between squamous epithelium and the dorsal respiratory (DR) and ventral respiratory (VR1) regions (slice a); between the DR/VR1 and dorsal olfactory (DO1) and ventral respiratory (VR2) regions (slice b); and the posterior DO2/VR2 regions (slice c). Similar divisions of nasal airways have been published by Frederick et al. (1998, 2002) and are redrawn here for (b) a male F344 rat and (c) a human. Major airflows designated by bold arrows.

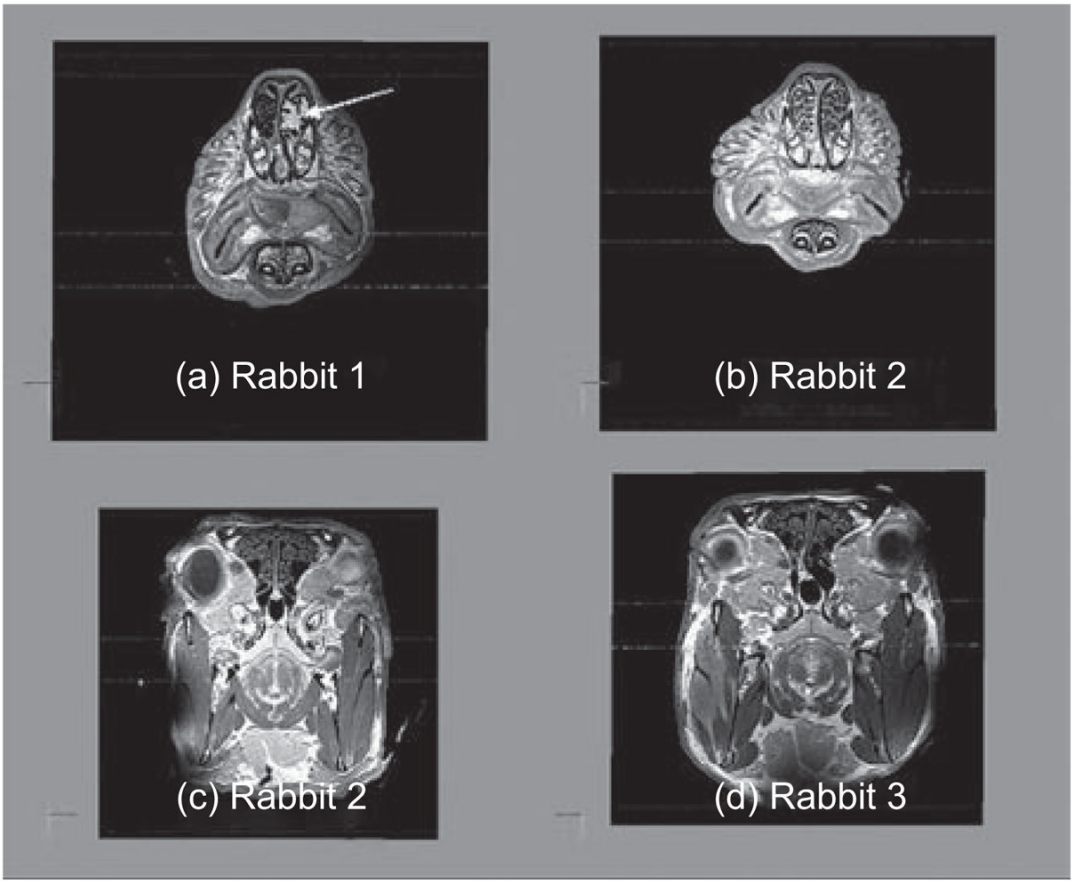

Figure 2.
Magnetic resonance imaging (MRI) cross sections through the maxilloturbinate region of rabbit 1 (a) and rabbit 2 (b) and the ethmoid turbinate region of rabbit 2 (c) and rabbit 3 (d). Note the presence of a mass in the left maxillary turbinate (designated by arrow) of rabbit 1 (a) and the asymmetry in the ethmoid turbinates of rabbit 3 (d) vs. rabbit 2 (c).

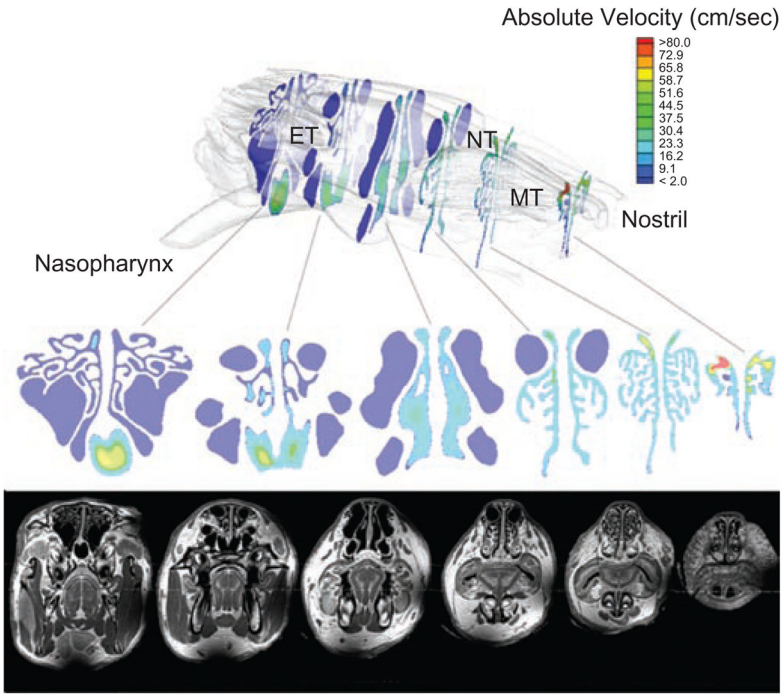

Figure 3.
Contour maps of airflows through various cross sections of the rabbit nasal airway (rabbit 3) with corresponding MR image. MT, maxil-loturbinates; NT, nasoturbinates; ET, ethmoid turbinates.

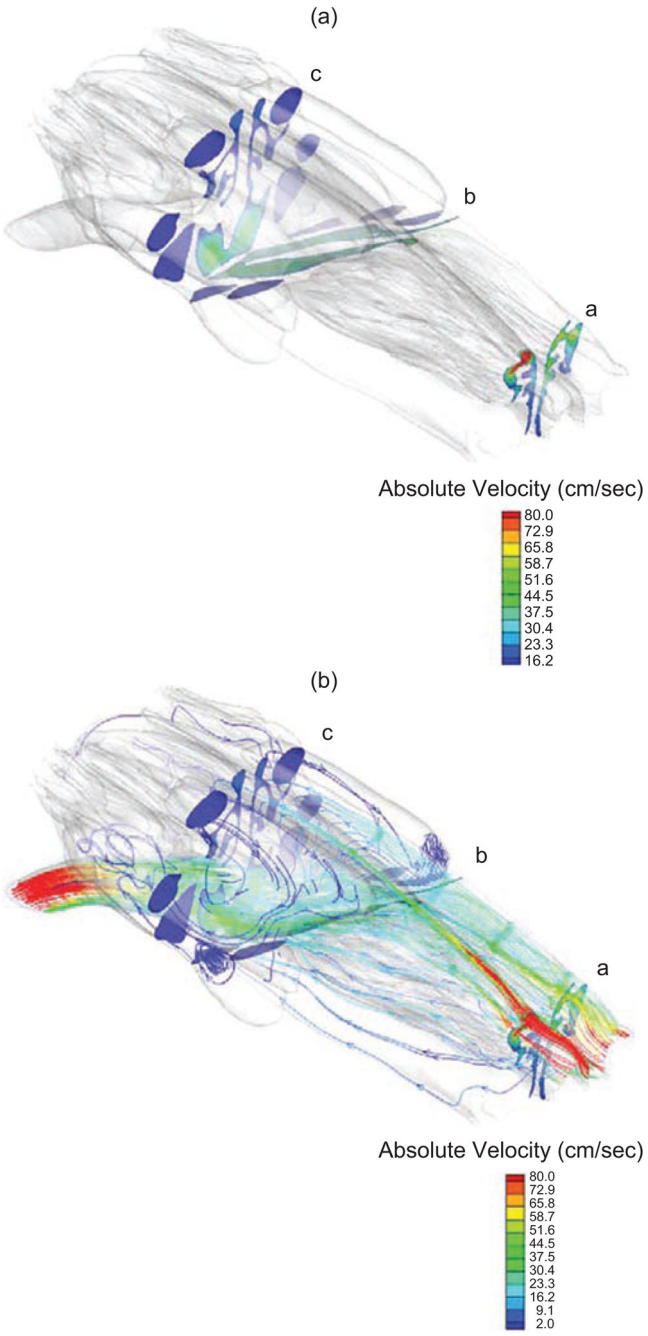

Figure 4.

(a) Cross sections with projected contour maps of the absolute velocity of air (cm/s) flowing through the *z* plane of the computational mesh of a rabbit nasal airway (rabbit 3) corresponding to each *z* slice depicted in (a) and (b) streamlines depicting airflow patterns determined from the CFD model at a steady-state inhalation of 680 ml/min.

Table 1

Nasal airway geometries for each female NZW rabbit.

Nasal airway geometries[a]				
Animal	**Body weight (kg)**	**Volume (cm^3)**	**Surface area (cm^2)**	**Length (cm)**
1	4.335	5.68	108.5	6.56
2	4.267	5.74	112.4	6.48
3	4.780	6.13	118.1	6.87
Mean ± SD	4.461 ± 0.279	5.85 ± 0.24	113.0 ± 4.8	6.64 ± 0.21

[a] Airway geometry (total volume, surface area, and length of the nasal airways) calculated from computational mesh (excluding nasopharynx).

Table 2

Nasal compartment surface areas, volumes, and percentages of total airflows entering each compartment defined in Figure 1 for each rabbit.

		Nasal region				
		Slice a		Slice b		Slice c
Rabbit	**Parameter**	**DR**	**VR1**	**DO1**	**VR2**[b]	**DO2**
1	Airflow split (% of total)[a]	82.4	17.6	49.4	50.6	0.2
	Surface area (cm^2)[b]	22.8	18.6	15.9	23.5	23.7
	Volume (cm^3)[b]	0.79	0.93	1.28	1.73	0.79
2	Airflow split (% of total)	96.5	3.5	50.1	49.9	1.5
	Surface area (cm^2)	26.0	15.2	16.3	20.3	26.6
	Volume (cm^3)	0.77	0.68	1.37	1.65	1.04
3	Airflow split (% of total)	95.9	4.1	42.8	57.2	1.5
	Surface area (cm^2)	29.1	15.7	17.9	22.3	29.4
	Volume (cm^3)	0.91	0.73	1.48	1.77	1.15
Mean ± SD	Airflow split (% of total)	91.6 ± 8.0	8.4 ± 8.0	47.4 ± 4.0	52.6 ± 4.0	1.1 ± 0.8
	Surface area (cm^2)	26.0 ± 3.2	16.5 ± 1.9	16.7 ± 1.1	22.1 ± 1.6	26.6 ± 2.8
	Volume (cm^3)	0.82 ± 0.08	0.78 ± 0.13	1.37 ± 0.10	1.72 ± 0.06	0.98 ± 0.17

[a] The airflow splits are calculated as the percent of the total mass flux entering each compartment across each cross-sectional or *z* slice shown in Figure 1. Total airflows that pass through each compartment are thus calculated as a mass balance of airflows that cross each *z* slice as well as across slices in the *x* plane bisecting the nasal airways into dorsal and ventral regions.

[b] Note that the sum of the surface areas and volumes for each compartment ignores the nostril, which is included in the totals presented in Table 1.